

**FACULTY
OF MATHEMATICS
AND PHYSICS**
Charles University

BACHELOR THESIS

Daniel Hofman

**Effect of substantial grain refinement on microstructure
and mechanical properties of precipitation hardenable
magnesium alloys**

Department of Physics of Materials

Supervisor of the bachelor thesis: RNDr. Peter Minárik Ph.D.

Study programme: Physics

Specialization: Applied physics

Prague 2019

I declare that I carried out this bachelor thesis independently, and only with the cited sources, literature and other professional sources.

I understand that my work relates to the rights and obligations under the Act No. 121/2000 Coll., the Copyright Act, as amended, in particular the fact that the Charles University has the right to conclude a license agreement on the use of this work as a school work pursuant to Section 60 paragraph 1 of the Copyright Act.

In Prague 1/4/2019

Daniel Hofman

First and foremost, I want to thank to Peter Minárik, for his unrelenting support and trust in this enterprise. I also want to thank Jana Kálová for helping me with sample preparation. Lastly I want to thank my parent for their support during my education.

Title: Effect of substantial grain refinement on microstructure and mechanical properties of precipitation hardenable magnesium alloys.

Author: Daniel Hofman

Department: Department of Physics of Materials

Supervisor: RNDr. Peter Minárik Ph.D.

Abstract: Properties of magnesium alloy WE43 and the effect of substantial grain refinement by ECAP were studied. The compressive strength test revealed a significant increase of yield strength after ECAP, resulting in yield strength of over 400 MPa after 8 ECAP passes. The material remained surprisingly ductile in both compression and tension. Thermal stability of the material was investigated via Vickers hardness test. The ultrafine-grained structure shows good thermal stability up to 300 °C, where the precipitates start to dissolve and grain size starts to increase, resulting in sharp fall of hardness. Annealing of the initial state showed best results for 210 °C where the precipitation hardening led to an increase in hardness up to ~101 HV.

Keywords: WE43, thermal stability, ultrafine grain, scanning electron microscopy, ECAP

Název práce: Vliv precipitačního zjemnění zrna na mikrostrukturu a mechanické vlastnosti precipitačně vytvrditelných hořčíkových slitin.

Autor: Daniel Hofman

Katedra: Katedra fyziky materiálů

Vedoucí bakalářské práce: RNDr. Peter Minárik Ph.D.

Abstrakt: V této práci byla zkoumána hořčíková slitina WE43 a vliv výrazného zjemnění zrna pomocí metody ECAP. Tlakové zkoušky ukázaly podstatné zvýšení pevnosti po aplikování metody ECAP, přičemž po osmy průchodech bylo dosaženo hodnoty přes 400 MPa. Navzdory této vysoké hodnotě pevnosti zůstal materiál velmi houževnatý, jak v tahu, tak v tlaku. Vyšetření teplotní stability materiálu bylo provedeno za pomoci měření mikrotvrdosti. Ultra jemnozrná struktura po 8 ECAP průchodech ukázala dobrou teplotní stabilitu do teploty 300 °C, kde se začaly rozpouštět precipitáty a souběžně začala růst velikost zrna, což vedlo k prudkému poklesu hodnoty mikrotvrdosti. Žihání výchozího stavu ukázalo nejlepší výsledky pro teplotu 210 °C, kde precipitační zpevnění vedlo ke zvýšení mikrotvrdosti až na ~101 HV.

Klíčová slova: WE43, teplotní stabilita, ultra jemné zrno, skenovací elektronová mikroskopie, ECAP

Table of Contents

1. Introduction	7
1.1 Magnesium	7
1.2 Magnesium alloy WE43	7
1.3 Corrosion.....	8
1.4 Equal channel angular pressing	9
1.5 Thermal stability of ultrafine-grained structure	11
2. Experimental methods.....	12
2.1 Experimental material.....	12
2.2 Optical microscopy.....	12
2.3 Scanning electron microscope	13
2.4 Backscattered electrons.....	13
2.5 Secondary electrons.....	14
2.6 Hardness	15
2.7 Compressive strength test	16
2.8 Tensile strength test	18
2.9 Annealing	19
2.10 Grain size.....	19
2.11 Measurement errors.....	20
3. Results	21
3.1 Initial state	21
3.2 WE43 Annealed.....	24
3.3 Compressive strength test	30
3.4 Tensile strength test	31
3.5 Hardness	33
4. Discussion.....	36
5. Conclusion.....	38
Bibliography	39
List of tables	41
List of figures.....	41
List of abbreviations.....	42

1. Introduction

1.1 Magnesium

Magnesium (Mg) has the lowest density of all metallic construction materials and forms a basis of multiple commercial alloys used in a variety of applications [1]. Due to its superior properties like high specific strength (strength of the material divided by its density), good castability, good weldability under controlled atmosphere, its ability to be milled at high speeds and the materials availability, a significant effort has been made to create alloys that would further enhance its properties. One of the main drawbacks of Mg is its limited corrosion resistance, along with its low melting point of 650 °C, making it unsuitable for applications in environments with elevated temperatures. Mg has a hexagonal close-packed (HCP) crystal structure, which limits its inherent ductility [2].

1.2 Magnesium alloy WE43

One of the most promising Mg alloys is WE43, which contains a small weight percentage of the following elements: Y (3.56%), Nd (2.20%), Zr (0.47%); and was homogenized for 8 hours at 525 °C (T4 treatment) and then quenched in water [3][4]. Its application is primarily based in automotive industry, aerospace industry and electronics, due to its low density and excellent mechanical properties, with extensive research and experimentation being focused towards potential medical use as biodegradable implants, with cardiovascular stents and orthopedic screws being already used in clinical practice. [5]

The aforementioned composition of {Mg, Y (3.56%), Nd (2.20%), Zr (0.47%)}, is often cited, some papers substitute Nd with RE (rare earths). It should be noted that Y is also a RE element [6], and since authors often attribute certain characteristics of the material to presence of RE in the

material, it often remains unclear whether Y is included in that statement as it is rarely stated explicitly.

Chemical analysis of as-cast WE43 showed that in addition to the elements denoted in the nominal composition a small weight percentage of Gd (0.78%) along with trace amounts of Al, Cr, Fe, Cu, Mn, Ni, Si and Zn were found [7]. Different phases have been observed in the material, with predominance of $Mg_{24}Y_5$ and $Mg_{41}Nd_5$ phases, with more recent studies finding other phases such as $Mg_3Y_{0.85}Nd_{0.15}$ (β'') disc-like precipitates, $Mg_{12}YNd$ (β') disc/globular precipitates, Mg_3RE (β_1) plate-like precipitates and $Mg_{14}YNd_2/Mg_5Nd$ (β) rod-like precipitates [8].

Magnesium alloys are one of the prospective materials for biodegradable implants such as cardiovascular stents and fixation pins, screws, wires, sheets, and plates. Biodegradation of the material removes the need for implant removal surgery, effectively halving the amount of procedures necessary. Biocompatibility of such a material is essential, with many magnesium alloys possessing excellent biocompatibility, with WE43 being one of the most promising ones, due to rare earth (RE) metals in the alloy providing increased corrosion resistance, hence reducing the biodegradation rate, which for WE43-based implants ranges from 12-24 months. Note that biodegradable implants, with cardiovascular stents and orthopedic screws have been successfully tested on animals and are currently being used in clinical practice [4].

A comparative study of *in vitro* and *in vivo* biocompatibility and rate of biodegradation showed that results from *in vitro* testing cannot be extrapolated to *in vivo* situations, with *in vitro* samples showing greatly increased rate of degradation of the material along with a noticeable formation of hydrogen bubbles on the surface of the sample [4]. The *in vivo* samples, after being implanted in mice for 2 months, showed no visible signs of degradation with small regions of oxidation being found with the use of magnification techniques. The surrounding tissue also showed no signs of hydrogen accumulation [4].

1.3 Corrosion

Corrosion of Mg alloys constitutes a substantial concern, as Mg is a base metal and exhibits high reactivity [9]. Mg and its alloys are prone to pitting corrosion, which occurs when metal is attacked locally by an aggressive solution, with chloride being the prime culprit, and leads to the formation

of small holes that propagate rapidly [10]. Pitting corrosion consists of three stages: 1) pit nucleation, 2) development of metastable pits, which either undergo repassivation or 3) grow into stable pits that propagate further through the material. A recent investigated pitting corrosion in Mg and WE43 and found that stronger protective layer incorporating the alloyed elements formed on the surface of the alloy, thus increasing its corrosion resistance [11].

1.4 Equal channel angular pressing

In order to refine grains to submicron levels, severe plastic deformation (SPD) techniques have been successfully utilized, one of which is equal-channel angular pressing (ECAP) [12]. The basis of grain refinement is thought to be realized by a formation of cells which, with increasing deformation further evolve into subgrains and finally to grains [13]. By refining the grains, we augment the grain boundary strengthening in the material, since grain size relates to yield stress as described by the Hall-Petch equation,

$$\sigma_y = \sigma_0 + \frac{k}{\sqrt{d}} \quad (1.1)$$

where σ_y is yield stress, σ_0 friction stress in an absence of grain boundaries, k is a material constant and d is grain size [14]. Grain refinement of Mg alloys thus leads to enhancement of their already exceptional specific strength (strength to weight ratio) which is especially desirable in aerospace and transportation industry.

Another process contributing to strengthening of the material is dislocation strengthening, which can be described by following equation,

$$\sigma = \langle M \rangle (\tau_0 + G\alpha b\sqrt{\rho}) \quad (1.2)$$

where σ is flow stress, $\langle M \rangle$ is average Taylor factor, τ_0 is thermal stress, α is geometrical factor, G is shear modulus, b is Burger's vector and ρ is dislocation density [14]. A study investigating several Mg alloys discovered that while dislocation density increased substantially after 1 ECAP pass in all 3 investigated alloys, further passes reduced the density, even below its original value.

The same did not hold true for grain size, which continued to decline until hitting minimum at which point the value remained somewhat constant [14].

The ECAP process often utilizes a die that contains a channel which bents by 90° (angle Φ) in the middle of the die. The angle Ψ represents the angle of the curvature and is usually 0° . Sample is then fitted into the channel and pressed through the by a plunger under high pressure. The process is illustrated in Fig 1.1. While processing FCC (face-centered cubic) materials by ECAP is relatively easy due to the multiplicity of active slip system, difficulties arise for HCP materials, due to the limited number of slip system they possess. If ECAP is performed at low temperature, the material usually develops cracks, but even when performed at high temperature a significant grain refinement is not achieved easily [15]. To combat this issue, a two-step process called EX-ECAP was introduced, where the grain size of the material was reduced by extrusion prior to the performing of ECAP. This process proved to be successful in achieving exceptional grain refinement in Mg alloys [15].

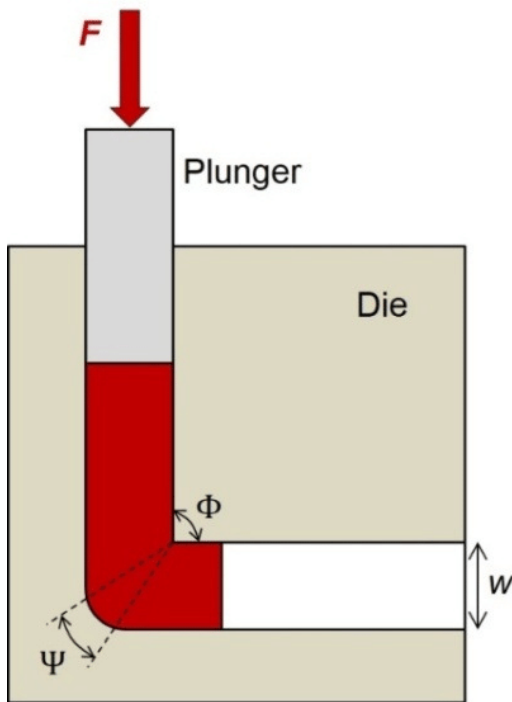


Fig. 1.1: Principle of ECAP.

1.5 Thermal stability of ultrafine-grained structure

While ultrafine-grained (UFG) structure has superior properties, its thermal stability is limited, since high density of grain boundaries is thermodynamically unstable. Elevated temperatures lead to grain growth and loss of mechanical strength. Thermal stability is affected by multiple factors such as phase composition, processing type, alloying elements, secondary phase particles or grain boundary types [16].

2. Experimental methods

2.1 Experimental material

WE43 AC was homogenized for 8 hours at 525 °C. Rectangular bars with dimension 10 x 10 x 100 mm³ were processed via ECAP 4 or 8 times, using the Bc route, rotating bar by 90° in the same direction after each pass. The process was performed at elevated temperatures (285-330 °C) at the speed of 5-10 mm/min using a die with Φ of 90° and Ψ of 0°. The resulting materials were labeled as WE43 4P (4 passes) and WE43 8P (8 passes).

2.2 Optical microscopy

WE43 AC was cut into multiple samples which were then encased in epoxy resin, allowing for easier manipulation as well as automated polishing, and were afterwards polished by a series of steps, starting with sandpaper, with an incremental lowering its roughness down to a grit of 4000 (3 μm), and ending with 0.25 μm colloidal silica. The sandpaper part of the polishing process was carried out with the use of water as the heat conductor, while in the latter part of the polishing when colloidal silica was used the water was replaced by ethanol, as to prevent oxidization of the surface. Upon reaching the desired polish, the samples were etched by a solution containing picric acid for 7 seconds. The as-cast state was photographed using optical microscope Olympus 6X 51. While optical microscopy allows us to observe grain structure of WE43 AC, it fails to do so for the 4P and 8P states, since the grain size of these states was found to be lesser than what the wavelength of visible light, which is the limiting factor, allows us to observe. If we take the mean wavelength of visible light to be 500 nm, the maximum resolution using optical microscopy would be around 1 μm. In order to further investigate the microstructure of the materials, we will have to use a microscope that operates on a lower wavelength – scanning electron microscope (SEM).

2.3 Scanning electron microscope

While optical microscope uses visible light as its means of obtaining information about a sample, the scanning electron microscope uses a beam of electrons which are emitted from an electron gun which possesses a wolfram filament cathode. Considering typical accelerating voltage of 10 kV (which was also used in our experiment), we can calculate the resulting De Broglie wavelength λ using the following non-relativistic formula,

$$\lambda = \frac{h}{\sqrt{2meV}} \quad (2.1)$$

which can be derived from well know relation between De Broglie's wavelength, Planck's constant and momentum [18]. The denotation of the symbols in the equation above is as follows: h is Planck's constant, m is electron mass, e is electron charge and V is accelerating voltage. The resulting wavelength is approximately 0.01 nm thus improving our resolution by up to five orders of magnitude. There are several types of signals produced by the interaction of the electron beam with the surface of a sample, with signal each having different interaction volume based on its energy and thus providing different information about the sample. We will be using only 2 types of signals - back-scattered electrons (BSE) and secondary electrons (SE) [18].

2.4 Backscattered electrons

BSE are high energy electrons that were reflected or back-scattered elastically by the atoms of the sample. The likelihood of the backscattering occurring is dependent on atomic number, with elements possessing higher atomic number being more likely to backscatter the incident electrons and thus appearing brighter than the ones with lower atomic number. Since BSE can only provide information about relative differences between the atoms constituting the sample, complementary methods such as X-ray spectroscopy are used when determining chemical composition of a sample, since X-ray spectroscopy determines specific elements contained within the sample (within the interaction volume) and each element can then be assigned to the specific area based on the brightness and atomic number.

BSE can be also used to observe channeling contrast, an effect caused by the existence of crystal structure within the sample. The depth to which an electron can travel is dependent on the angle between the incident beam and the crystal structure along its path. If the direction of travel of incident electrons is close to being parallel to the predominantly populated crystallographic planes, the penetration will be much higher than it would be for a random orientation, and thus the amount of backscattered electrons will be much lower. The principle can be seen in Fig. 2.1. If incident electrons encounter a crystal defect along their path, such as dislocation or stacking fault, the backscattering will increase significantly and the defect will be displayed as a bright spot on a darker background [18].

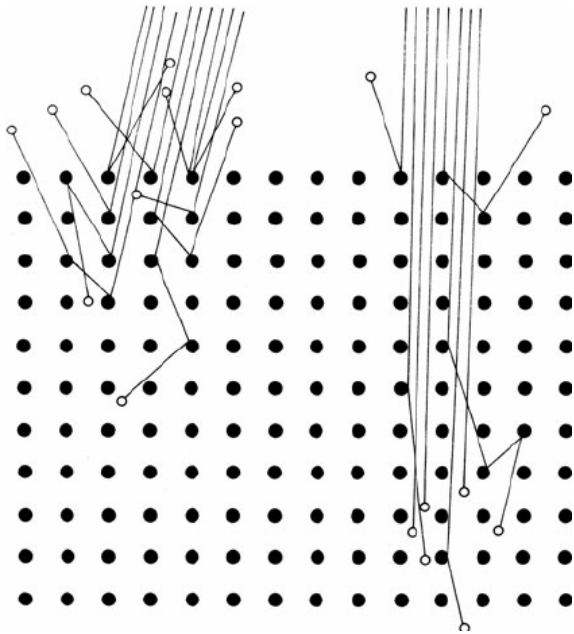


Fig. 2.1: Principle of channeling contrast – general orientation of crystallographic planes to incident electron (left) vs. parallel orientation (right).

2.5 Secondary electrons

SE are low energy electrons originally belonging to atoms of the specimen, which are ejected from their shells due to an inelastic scattering interaction with the beam electrons. Since these ejected electrons have very low energy (<50 eV), they can be collected via a positively charged grid, which is generally placed at the side of the sample, in comparison with the BSE detectors, which have to

be placed around the field gun. Another result of their low energy is that the interaction volume as well as penetration depth is very low, making the signal highly responsive to changes in surface uniformity (protrusions or cavities) and thus providing us with topographic contrast [18].

The microstructure of AC, 4P, 8P and AC annealed for 8 hours at 250°C (T5 treatment) [23] was investigated using scanning electron microscope (SEM) Zeiss AURIGURA Compact equipped with EDAX EDS (energy-dispersive X-ray spectroscopy). The samples for SEM were prepared akin to the samples for optical microscopy, with the exception of the etching process, which was skipped.

2.6 Hardness

In order to examine material's ability to resist plastic deformation, a hardness test can be performed. One of the most widespread methods of such testing is the Vickers hardness test, which in our case will be performed using Microhardness Tester Qness Q10 A+. The way in which the measurement is realized is as follows: a diamond indenter in the shape of a square-based pyramid is pressed into the material by a predetermined force based on a set of available loads. The opposite sides of the pyramid are situated so that the angle between them is 136° as it was experimentally found that with this setting the result remains independent of the load used [19]. The area of the indentation A can be calculated using the following equation,

$$A = \frac{d^2}{2\sin(136^\circ/2)} \quad (2.2)$$

where d is the length of the diagonal of the indentation. The unit of hardness of the Vickers hardness test is Vickers Pyramid Number (HV). It is calculated by dividing the force F applied on the indenter by the area of the indentation, as can be seen in the following equation.

$$HV = \frac{F}{A} \approx \frac{1.8544F}{d^2} \quad (2.3)$$

Note that d is in millimeters and force F in the equation is in kfg (kilogram-force) so if one wants to obtain the hardness in Newtons, one has to divide the force by the gravitational acceleration [20].

2.7 Compressive strength test

In order to investigate resistance of a material to compression, compressive strength test shall be performed. The test comprises of a sample in a shape of rectangular cuboid, which is sufficiently polished and inserted between the jaws of a universal testing machine, in our case INSTRON 5882, and is put under an increasing amount of load until a failure in the material occurs. The failure most commonly manifests as a clean break in the material that is angled 45° to the force applied, which is explained by Schmid's law where the minimal force required for slip in a material is determined by a maximizing the term $\cos(\alpha)\cos(I-\alpha)$ known as Schmid factor, with α being an angle between the slip direction and the force applied on the sample, which reaches maximum for an angle of 45° [25].

Upon completing the test, we receive information about engineering stress σ_e which is defined by the following equation,

$$\sigma_e = \frac{F}{A_0} \quad (2.4)$$

where F is applied load and A_0 is the original specimen area to which the load was applied [21].

We can also receive the values of engineering strain ε_e which is defined by the following equation,

$$\varepsilon_e = \frac{l - l_0}{l_0} \quad (2.5)$$

where l is the current length of the specimen and l_0 is the original length of the specimen.

These quantities however do not take into account the changes in shape that the specimen is subjected to during the test. The quantities that do take that into account are called true strain and true stress.

To obtain true stress, we postulate that the volume of a sample remains constant throughout its deformation and thus we can write that $Al = A_0l_0$. We can rewrite the equation for engineering stress, substituting it with true stress as follows,

$$(2.6)$$

$$\sigma_T = \frac{Fl}{A_0 l_0} = \sigma(\varepsilon + 1)$$

since we know that $l/l_0 = \varepsilon + 1$ from equation (3.5).

To obtain true strain, we can substitute the change of the sample length ($l-l_0$) by the infinitesimal change dL , as well as the original length l_0 by immediate length L and integrate from l_0 to l , as shown by the following equation,

$$\varepsilon_T = \int_{l_0}^l \frac{1}{L} dL = \ln \frac{l}{l_0} = |\ln(\varepsilon + 1)| \quad (2.7)$$

where we use the same substitution for l/l_0 from equation (3.5) as in the previous formula.

Once we know true strain and true stress, we will plot them into a graph to obtain the stress-strain curve, from which we can obtain yield stress which is defined as the point of onset of a plastic deformation of the material, where prior to this point the material will deform elastically by stretching of the atomic bonds and will return to its original state once the load is removed. Since determining the exact point of the onset of plastic deformation is extraordinarily difficult, the offset yield point was introduced as a value of stress at the length of the material changes by 0.2% from its original length, in other words 0.2% change in ε , and the value of stress for 0.2% ε is referred to as yield strength. In order to properly determine the aforementioned yield strength, the linear part of the stress-strain curve (the part following Hooke's law) must be fitted with a straight line and its parallel must be drawn with a shift of 0.2% ε , which would be 0.002ε for stress-strain curve that follows Hooke's law from the point of origin (0,0). If that is not the case, which may be caused by unevenness of the sample, or the jaws, as well as the sample not being properly positioned/loaded, especially in the case of tensile strength test, the shift will be 0.002ε plus the value of ε at the point of intersection of the fitted line with the x-axis.

The samples for the compressive strength test were cut to into a shape of rectangular cuboid, with an emphasis on the width and height to be as similar as possible, thus creating a square shaped face, which will bear the load. The samples were then polished with sandpaper down to a roughness of 2000. Increased attention and effort was given to ensure the orthogonality of the samples. The final dimensions of the samples were between 4.5-6mm length and 3.5-4mm height and width, depending on the amount of raw material left thus the differences were predominantly between different-material samples, with the samples from the same material having close to identical dimensions. The samples from materials WE43 AC, WE43 4P and WE43 8P were tested, along with an annealed state of WE43 AC, which has been kept at 250 °C for 16 hours (T5 condition)[23].

2.8 Tensile strength test

Similarly to the compressive strength test, the tensile strength test tests the material's resistance to applied force, this time in the opposite direction. The test it performed on the same testing machine, however the jaws are replaced with vises. In addition, the sample must be installed into grips and further secured by substantially tightened screws. The sample has to be milled into a specific bone-like shape (see Fig 2.2). All previous equations for strain and stress will still apply. The yield strength will also be acquired by the same series of steps as for compression. Note that only the milled part of a sample constitutes the length of the sample since the non-milled part has greater area and thus the stress will be proportionately lower (see equation 3.4).

WE43 AC bar was milled and then cut into samples of the required shape, with its length and width being approximately 7 mm and 4 mm respectively. The samples were then polished by sandpaper down to a grit of 2000 resulting with a resulting thickness of 0.6-0.8 mm, and were thereupon tested.

Note that deformation speed $\dot{\epsilon}$ for both compressive and tensile strength was equal to 10^{-3}s^{-1} .

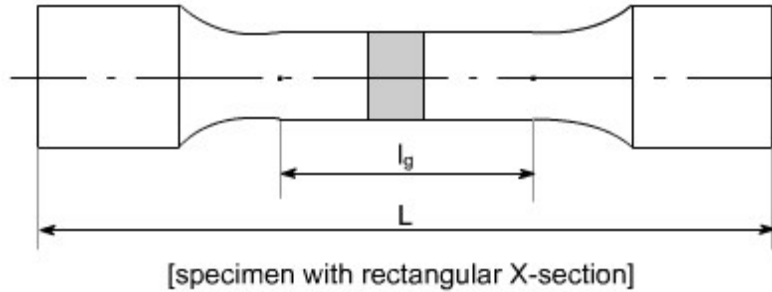


Fig. 2.2: Tensile strength test specimen.

2.9 Annealing

Annealing refers to a heat treatment of a material with the purpose of enhancing its mechanical properties. The material is held above its recrystallization temperature for a certain period of time and is cooled afterwards. Increased temperature releases internal stress that was introduced to the material, in our case by severe plastic deformation, and allows for greater mobility of atoms, possibly resulting in formation, or increase in density of precipitates. The heating and cooling rate affect phase composition and grain size. Higher temperatures also allow for easier movement of dislocations, thus reducing the overall number of dislocations in the material. Annealing generally leads to a small decrease in hardness and a profound increase in ductility [22].

Samples of AC and 8P states were polished down to a grit of 4000 and subsequently subjected to isochronal and isothermal annealing. The AC state was annealed isothermally at 210 °C and 250 °C with the time period ranging from 1 hour to 7 days. The 8P state was annealed isothermally at 250 °C, with the period being 2, 4, 8 and 16 hours, and also isochronally for 1 hour with the temperature ranging from 160 °C to 500 °C. Upon reaching the desired duration of annealing, the samples were quenched in a bucket of water and prepared for the Vickers hardness test.

2.10 Grain size

In order to determine grain size, we will use the circle method, where we will construct a circle on the photograph of the sample and calculate the number of grains it intersects. We will then use the following formula, (2.8)

$$d = \frac{3\pi D}{2n}$$

where D is diameter of the circle, n is the number of intersected grains and d is grain size [17].

2.11 Measurement errors

All measurement errors were calculated as follows, unless stated otherwise; standard deviation SD was calculated using the following formula,

$$SD = \sqrt{\frac{\sum_{i=1}^n (x_i - \bar{x})^2}{n - 1}} \quad (2.9)$$

where x_i is the value of the quantity, \bar{x} is the mean of x_i and n is the number of data points.

The total error μ is calculated using following formula,

$$\mu = \sqrt{SD^2 + EE^2} \quad (2.10)$$

where EE is error of value measured by the equipment which we will in our case take as a 1% of the measured value.

3. Results

3.1 Initial state

The photo from optical microscopy (Fig 3.1) shows a typical grain structure with high density of high-angle grain boundaries (grain misorientation angle $>15^\circ$).

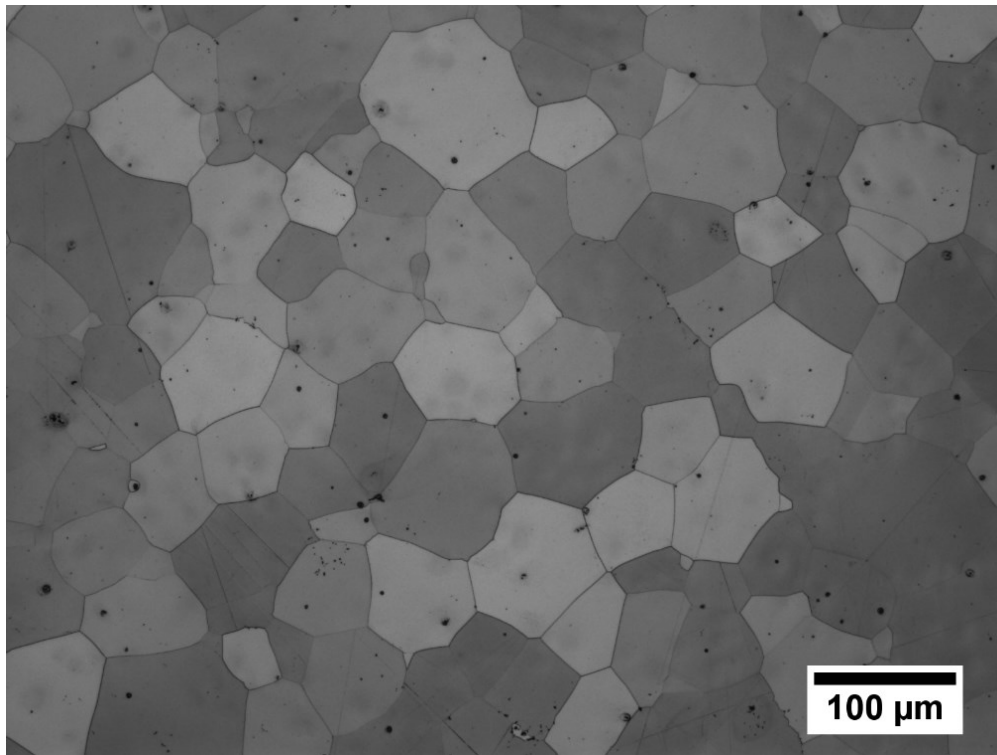


Fig. 3.1: WE43 AC photographed using optical microscopy.

In order to study microstructure of the samples BSE signal was used with an accelerating voltage of 10 kV. The SEM images of WE43 AC show not only the grain structure (Fig 3.2a), but also undissolved particles of Zr (Fig 3.2b), as well as pockets containing Si and C (Fig 3.2d), which were most likely introduced into the material during its production. Partially dissolved Zr particles can be observed in Fig 3.2c. The neighboring areas are brighter due to the predominance of Zr particles that raise the average atomic number in the area.

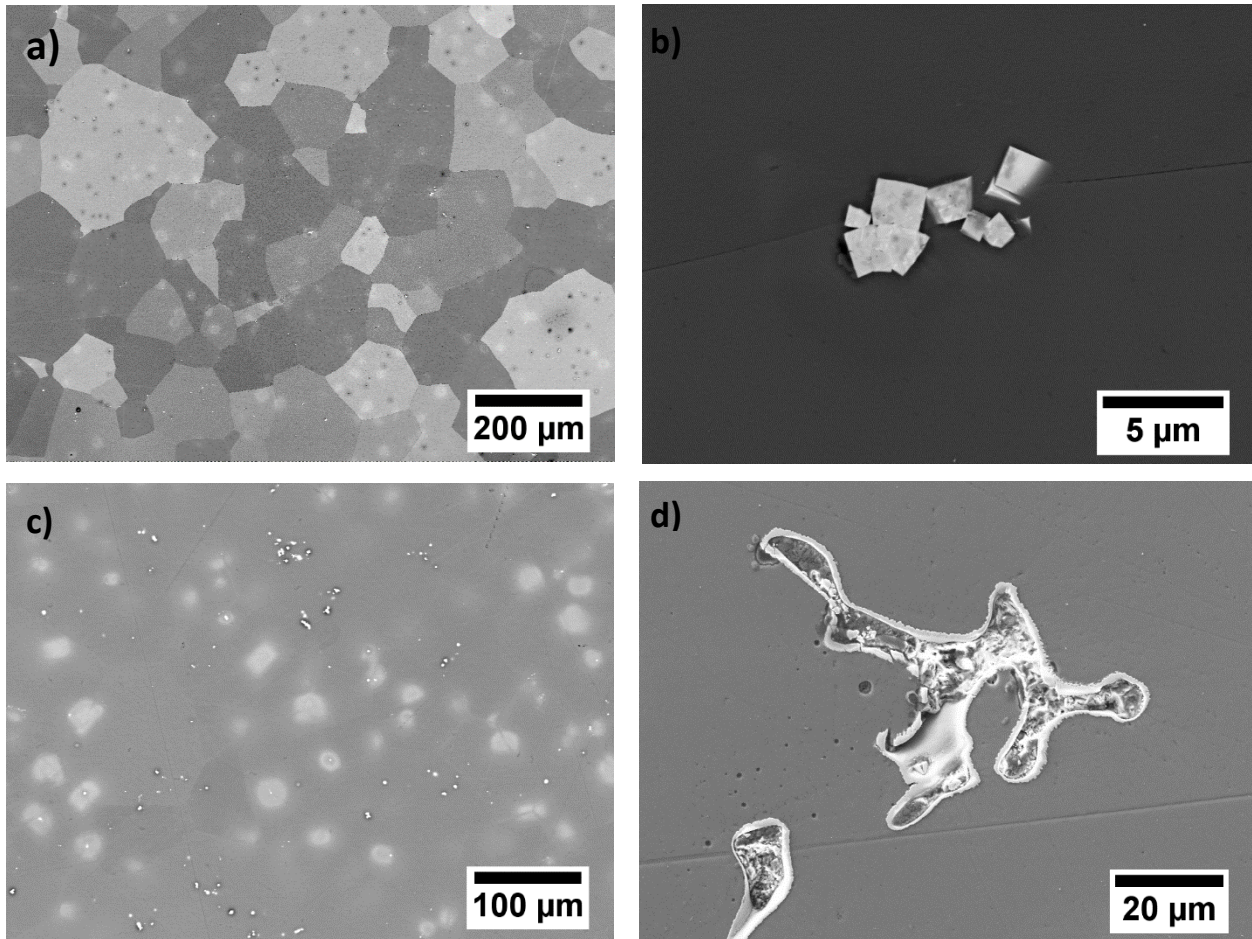


Fig. 3.2: SEM images of WE43 a) grain structure b) undissolved Zr particles c) partially dissolved Zr particles, d) pocket containing Si and C

Images of 4P state show much finer grain structure with copious amounts of precipitates present (Fig 3.3a), as well as lamellas having been formed inside the grains (Fig 3.3b), and a higher density of precipitates being located in grain boundaries (Fig 3.3c). While some particles of undissolved Zr are still present, their concentration has been reduced significantly. The 8P state shows further reduction in grain size with greatly homogenized structure containing extraordinarily high amount of precipitates (Fig 3.4a and b), Precipitates can be seen in more detail in Fig 3.5.

Grain size of WE43 AC was calculated using the circle method. Photos from optical SEM as well as optical microscopy were used. The resulting grain size calculated from formula (2.8) was $115 \pm 45 \mu\text{m}$.

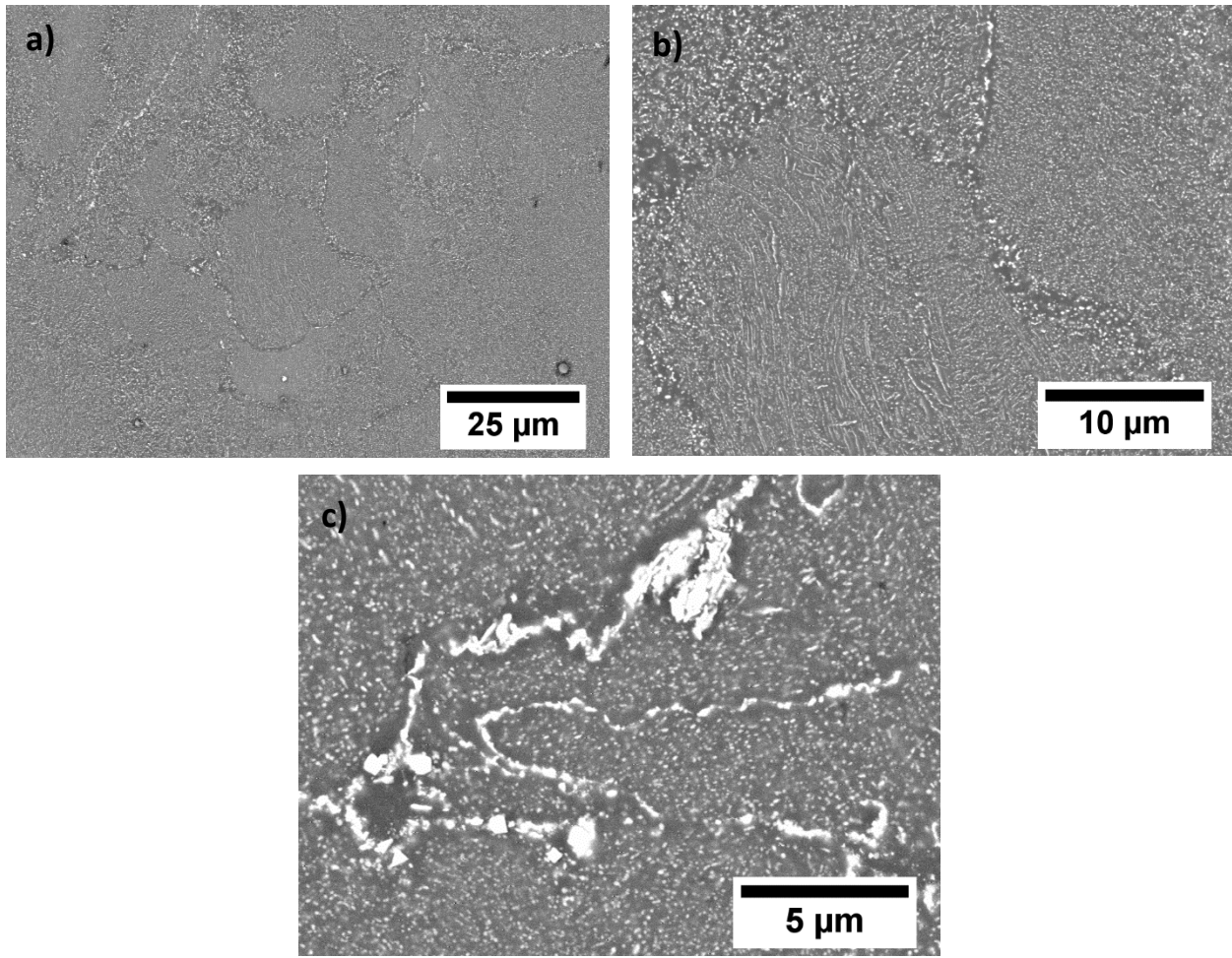


Fig. 3.3: SEM images of WE43 4P.

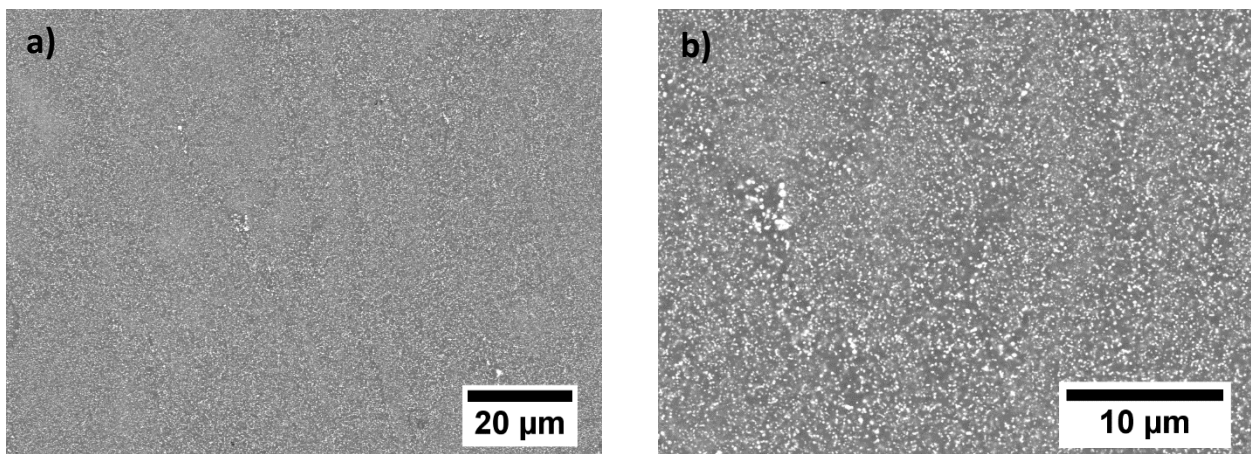


Fig. 3.4: SEM images of WE43 8P.

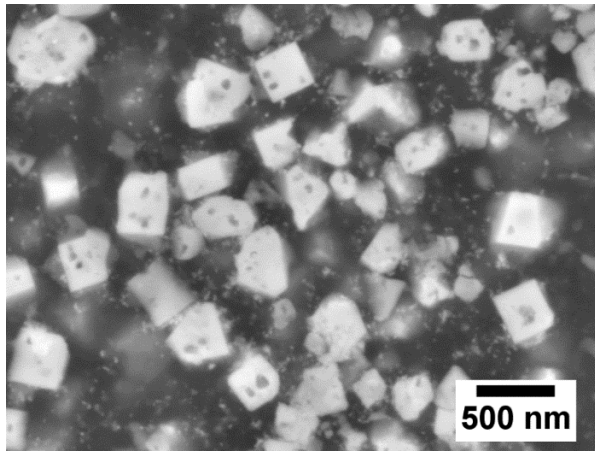


Fig. 3.5: Detail of Zr particles in WE43 8P.

A photo of WE43 8P was obtained using transmission electron microscopy (TEM) (Fig. 3.9). The photo was obtained using bright field illumination, along with selected area electron diffraction pattern (SAED) [24]. The composition of precipitates located predominantly along grain boundaries was found to be Mg_5RE possessing FCC structure.

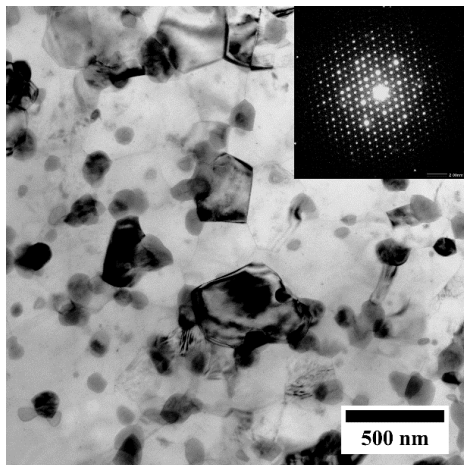


Fig. 3.6 TEM image of WE43 8P sample (bright field) with SAED pattern of Mg_5RE .

3.2 WE43 Annealed

In comparison with the solid solution state, just 4 hours of annealing at 210 °C isothermally shows great differences – almost all Zr particles have either dissolved into the matrix, or formed precipitates that are starting to gravitate towards grain boundary (Fig. 3.6a). At 24 hours, the precipitates have filled the grain boundary and a small number of lamellas was formed (Fig. 3.6b).

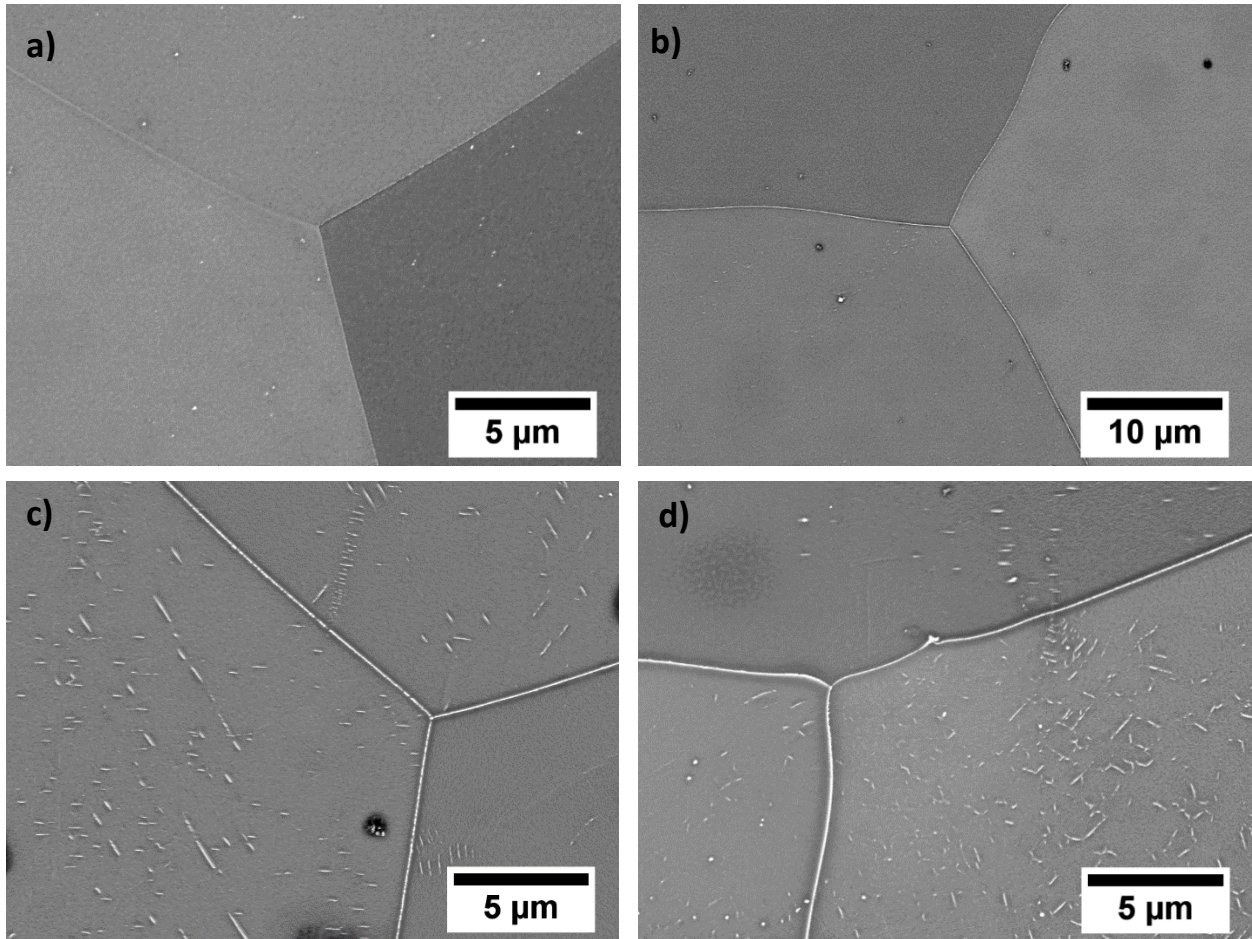
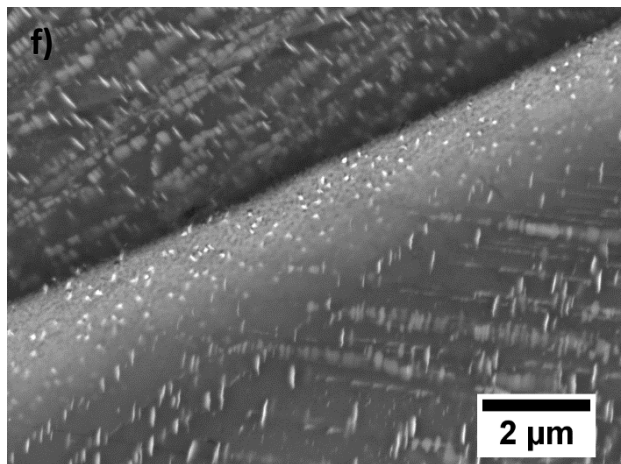
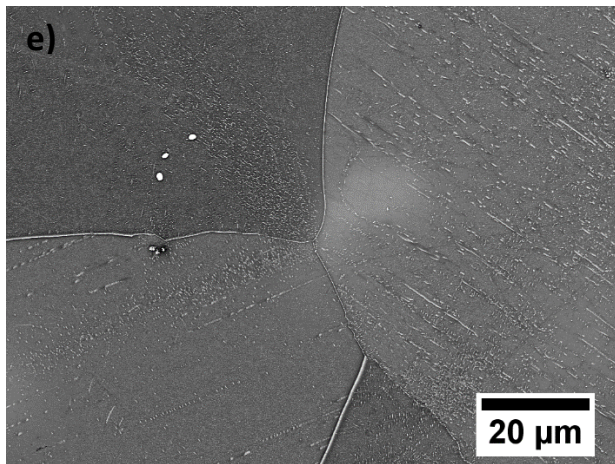
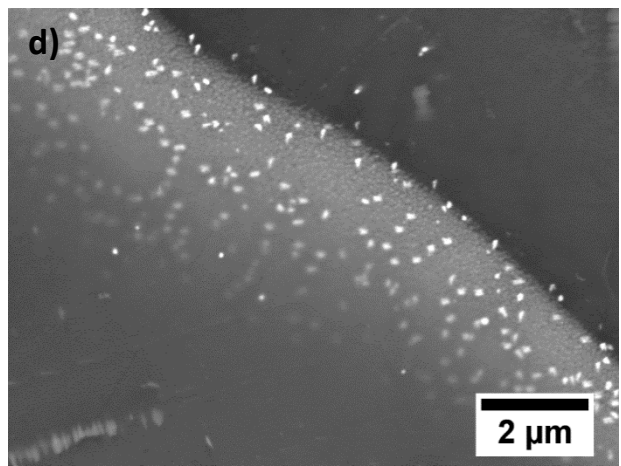
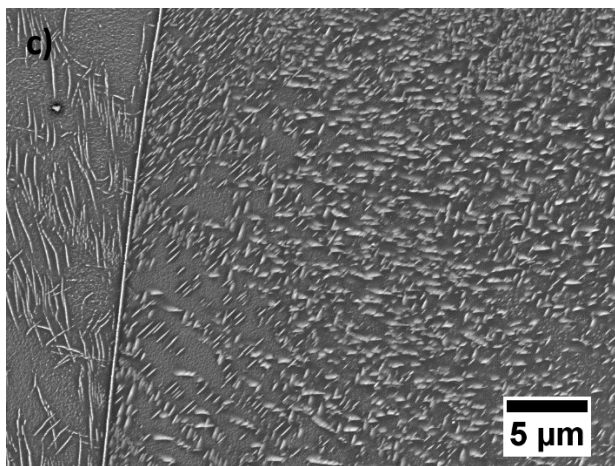
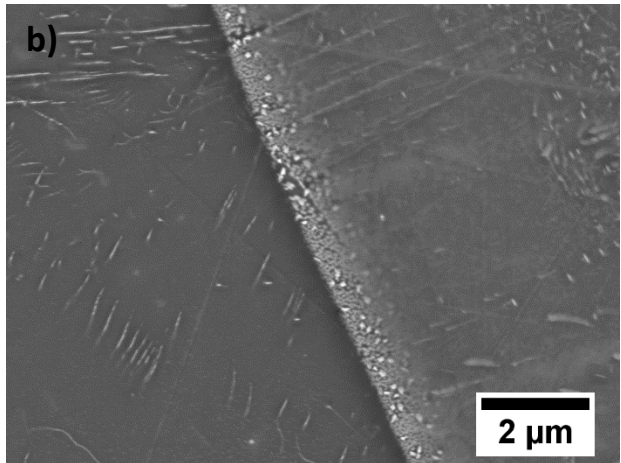
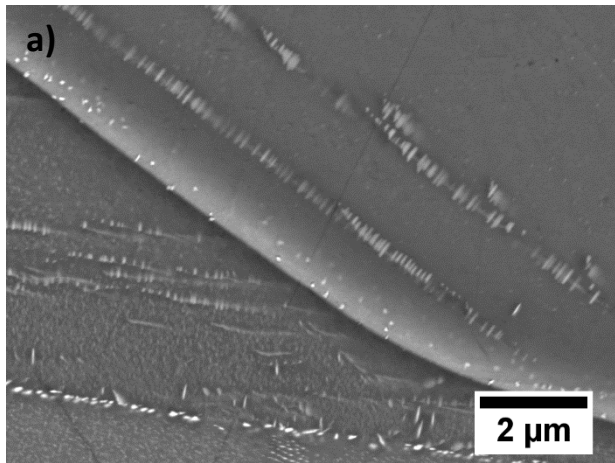
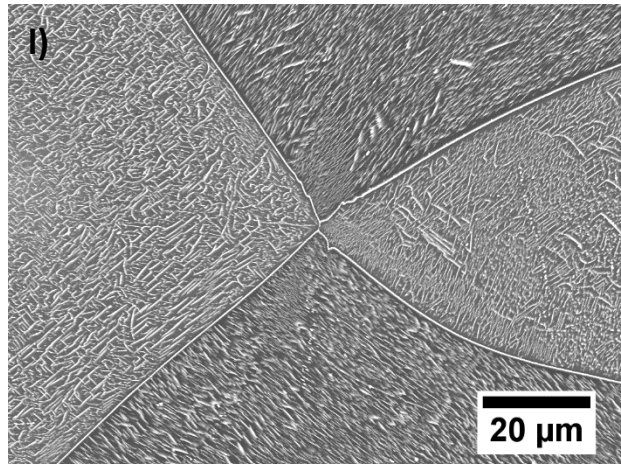
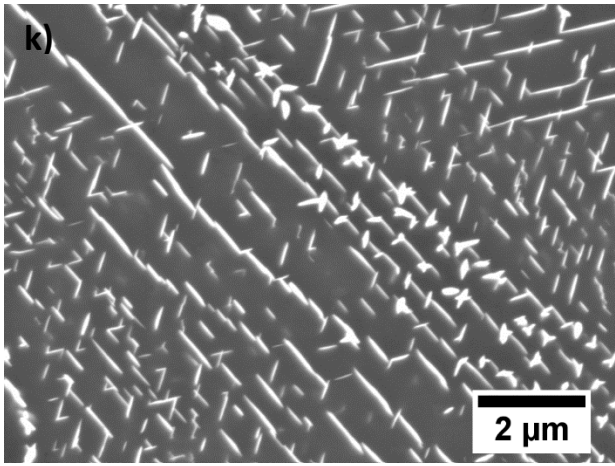
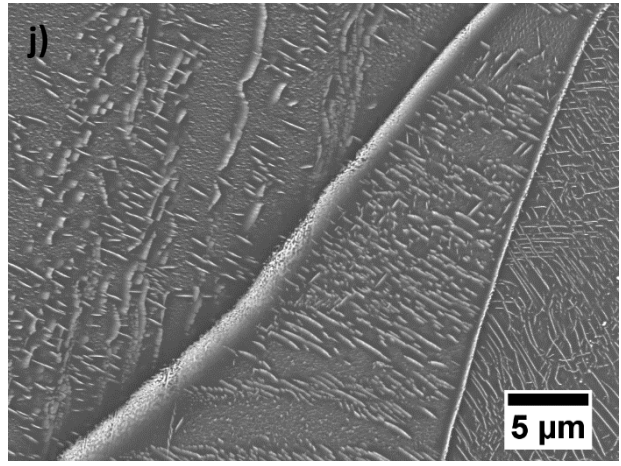
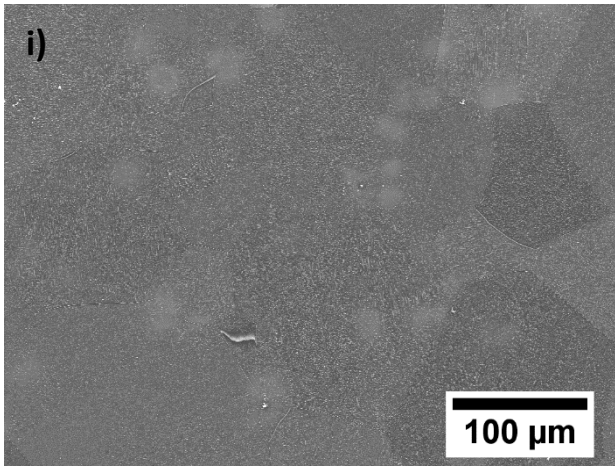
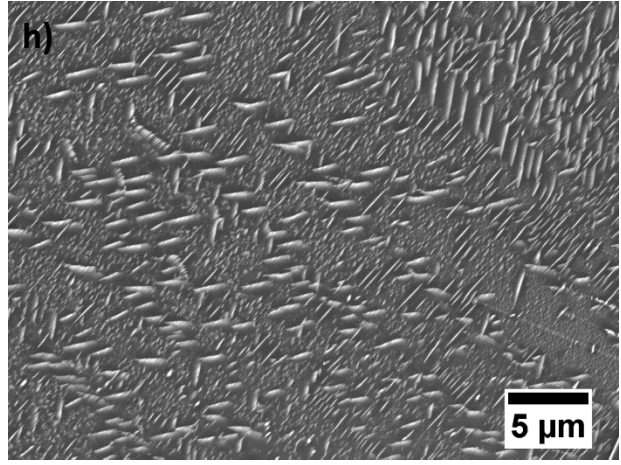
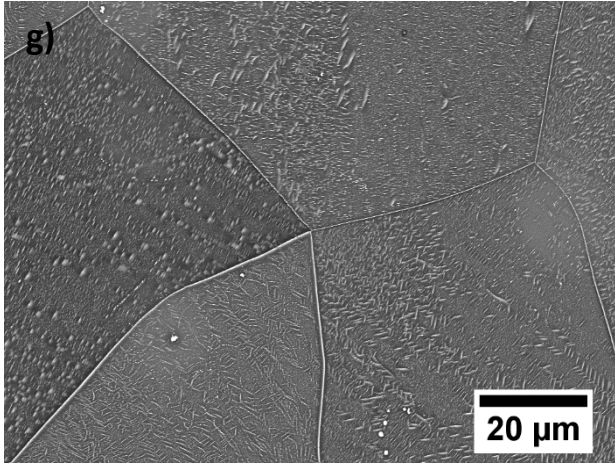


Fig. 3.7: WE43 isothermally annealed at 210 °C for a) 4 hours b) 24 hours c) 96 hours d) 168 hours.

The 4 days photo shows an increase in the lamellas formation (Fig. 3.7c), which is further propagated, as seen on the 7 days photo (Fig. 3.7d).

Annealing at 250° isothermally shows a fairly substantial lamellar formation after just 1 hour of the annealing (Fig. 3.8a). We can see the gravitation of precipitates into the grain boundary after only 2 hours (Fig. 3.8b), which further intensifies, as seen on the 4 hour photo (Fig. 3.8d). We can also observe precipitates beginning to cut the lamellas (Fig. 3.8c). These trends continue as seen on the 8 hour photographs (Fig. 3.8e and f) and at 16 hours we can see the grain boundary filled with precipitates as well as lamellas intersecting each other (Fig. 3.8g and h). With ever-increasing amount of precipitates, the structure begin to attain homogeneity, as can be seen in Fig. 3.8i with the grain boundary overflowing with precipitates (Fig. 3.8j).





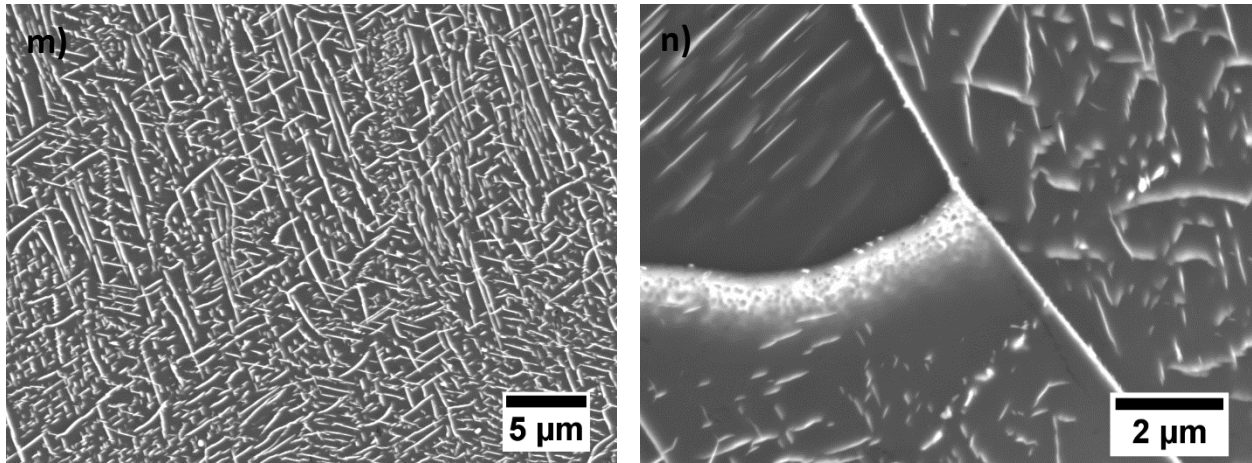


Fig. 3.8: WE43 AC annealed at 250 °C for a) 1h b) 2h c),d) 4h e,)f) 8h g),h) 16h i),j) 24h k) 48h l),m),n) 168 hours.

The amount of lamellas in zig-zag formation (the disc-shaped phase precipitates in along prismatic planes which intersect under 30° angle) keeps increasing as seen in the 48 hours photo (Fig. 3.8k), and material keeps increasing its homogeneity, however the rate drops significantly past the 24/48 hour mark. Since the change in the material during the 3-7 day annealing period is very gradual only the final state is displayed here, showcasing the precipitates' homogeneity in Fig 3.8l, detail of the lamellas in Fig. 3.8m and the grain boundary in Fig. 3.8n.

Annealing of WE43 AC isochronally for 1 hour shows similar progression, as most of the Zr particles are not dissolved at 220 °C, with no visible precipitates present (Fig. 3.9a). At 300 °C the precipitates start filling up the grain boundary and less Zr particles are left undissolved (Fig. 3.9b), while the formation of lamellas begins (Fig. 3.9c). Lamellas start appearing with a substantial increase at 360 °C with grain boundary being filled with precipitates (3.9d). At 400 °C one can observe lamellas intersecting at elevated rate (Fig. 3.9e) and grain boundary overflowing with precipitates (Fig. 3.9f).

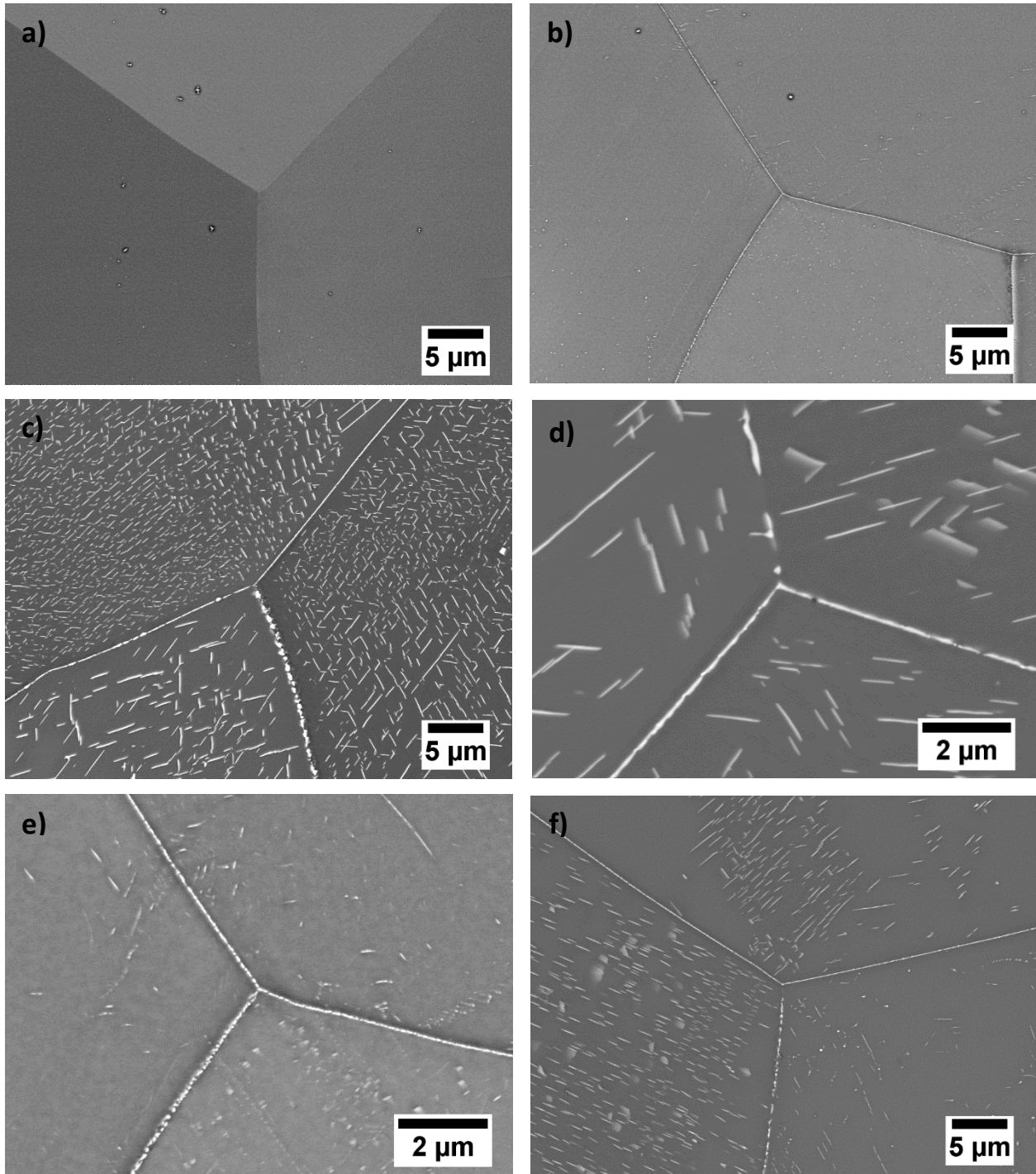


Fig. 3.9: WE43 AC annealed for 1 hour at a) 220 °C b),c) 300 °C d) 360 °C e),f) 400 °C.

3.3 Compressive strength test

WE43 AC, 4P and 8P states were tested, along with AC state annealed for 16 hours at 250 °C (T5). We can observe massive increase of yield strength both by annealing when comparing the AC state with the annealed one, as well as by severe plastic deformation introduced into the material (ECAP), with 4P and 8P states.

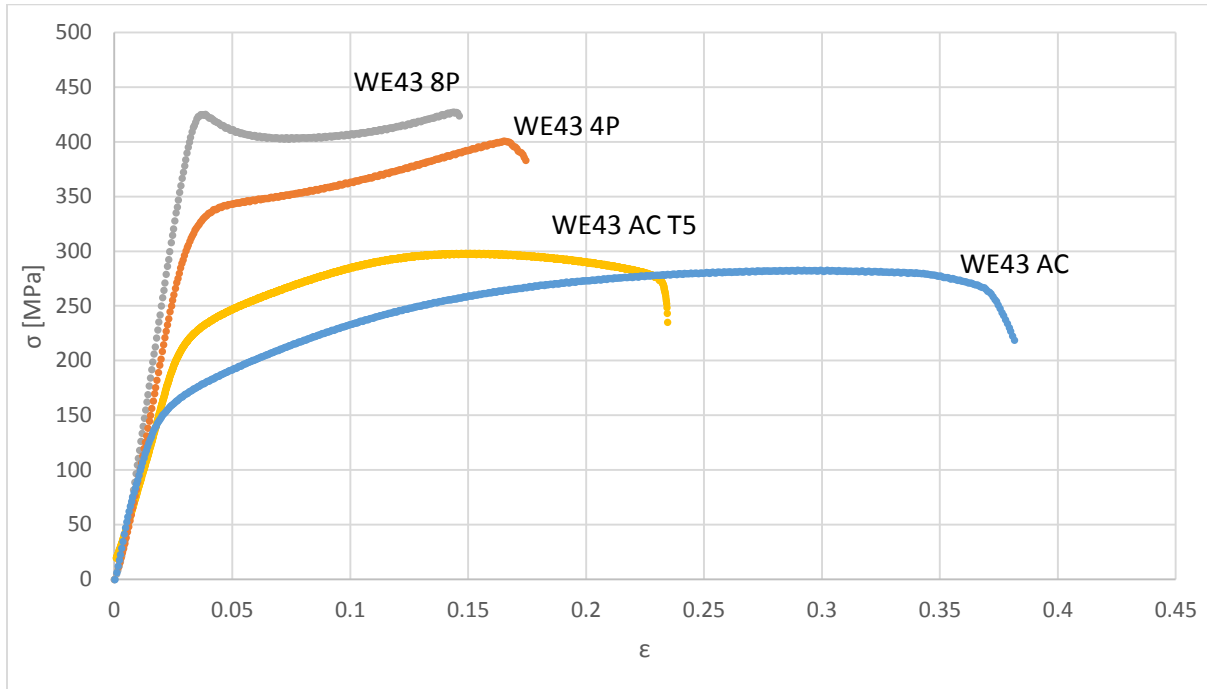


Fig. 3.10: Stress-strain diagram (compression) for WE43 AC, 4P, 8P and WE43 AC T5.

Table 1: Yield stress of tested materials in compression.

	σ [Mpa]
AC	126 ± 16
4P	310 ± 9
8P	412 ± 10
AC T5	202 ± 10

3.4 Tensile strength test

WE43 8P state was tested with the resulting yield strength being 364 ± 7 MPa.

The specimen used in the test was investigated using SEM by SE signal. Typical plastic deformation was observed with no specific area of failure. The photos show one particle in each dent, which were pulled by the deformation as they impeded the dislocation movement and caused cavitation in the final state.

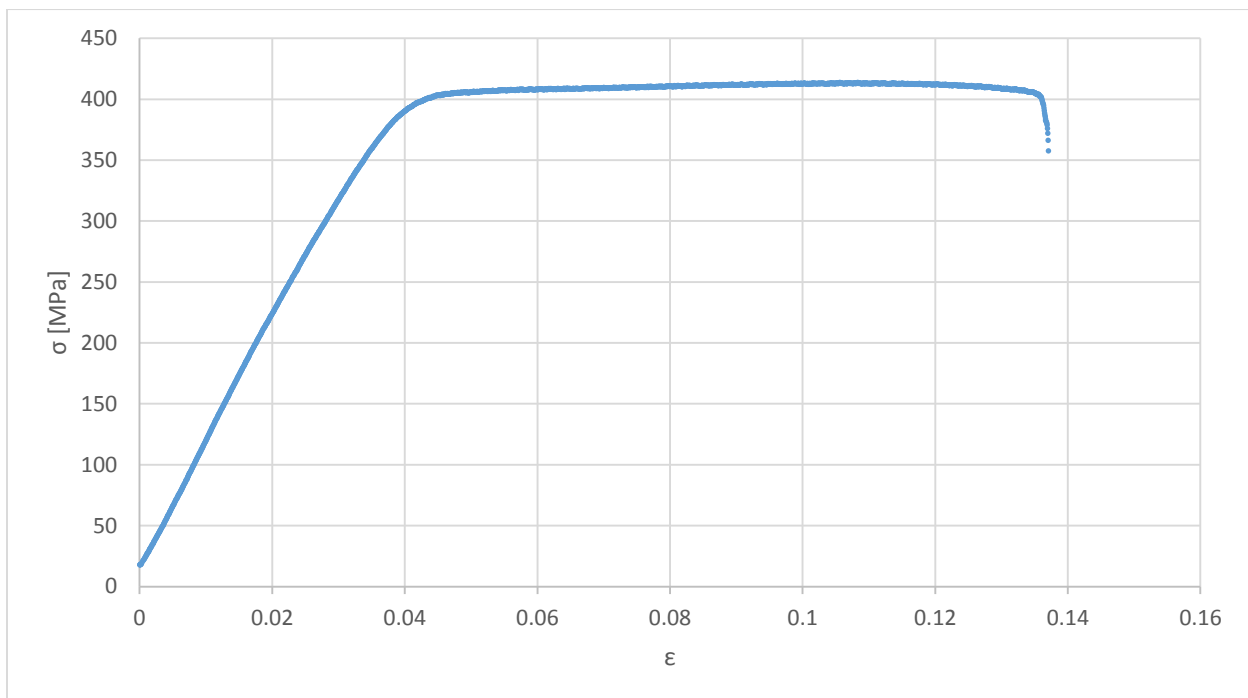


Fig. 3.11: Stress-strain diagram (tension) for WE43 8P.

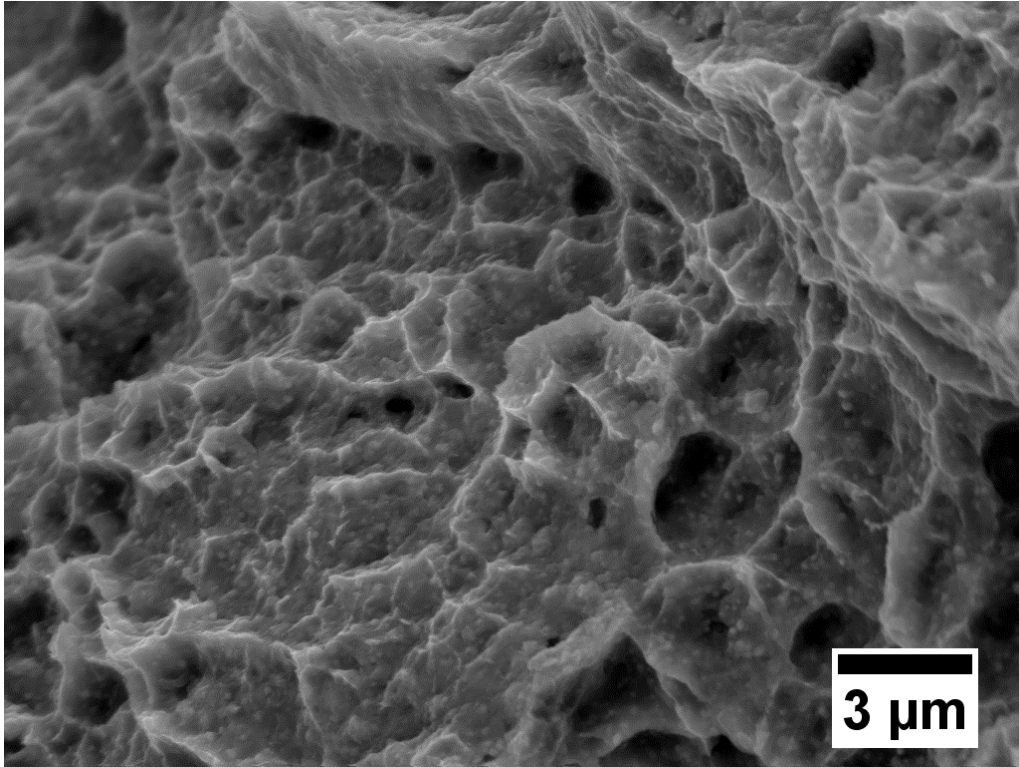


Fig. 3.12a: SEM photo of a plastically deformed WE43 8P.

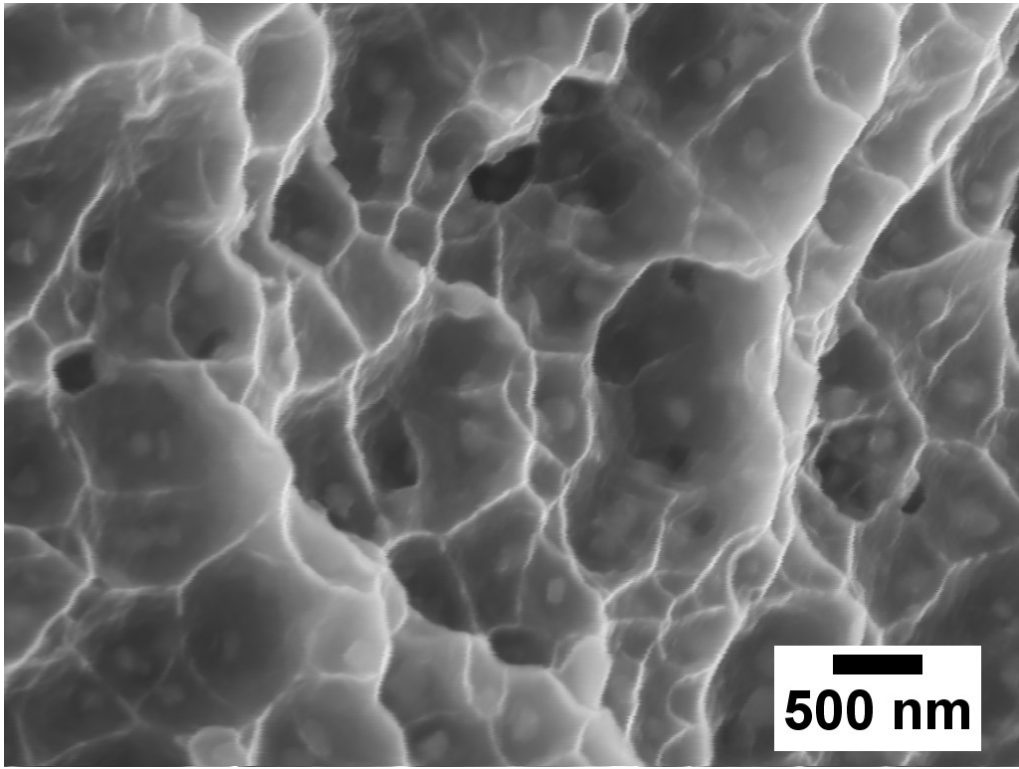


Fig. 3.12b: Detailed SEM photo of a plastically deformed WE43 8P.

3.5 Hardness

WE43 AC and WE43 8P were annealed and their hardness was tested by Vickers hardness test. WE43 AC was annealed isothermally at 210 °C (Fig 3.13) and 250 °C (Fig 3.14) for 7 days. At 210°C the maximum hardness was reached at 3 days at 101.2 HV, whether for 250 °C the maximum value was at 8 hours. Since standard deviations of both maximums are fairly large compared to the difference between values for other times, one cannot proclaim with certainty that the times for which the maximums were found are the general maximums.

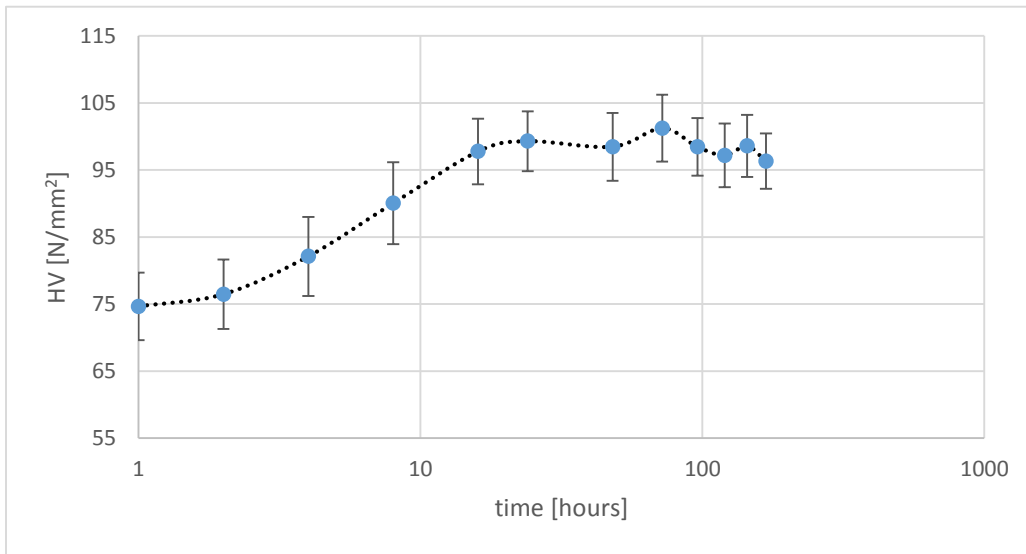


Fig. 3.13: Hardness of WE43 AC annealed at 210 °C.

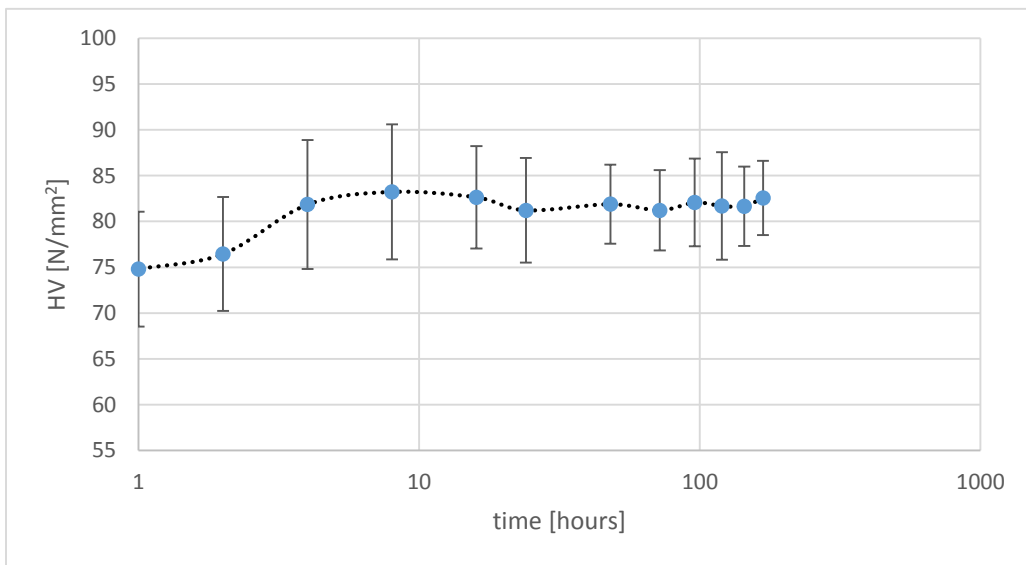


Fig. 3.14: Hardness of WE43 AC annealed at 250 °C.

WE43 8P was annealed isothermally at 250 °C from 2 to 16 hours (Fig. 3.15) with the maximum being 2 hours at 115.2 HV. It was also annealed isochronally for 1 hour from temperatures 160 °C to 500 °C (Fig. 3.16). First measurement used a load of 100 g which proved to be insufficient as the grain size was similar to the size of the indentation. Thus the 500 g load was used, which was used for all other measurements, and a maximum HV of 119.2 was achieved at 280 °C. The hardness then sharply falls after 300 °C, recovering slightly around 460 °C.

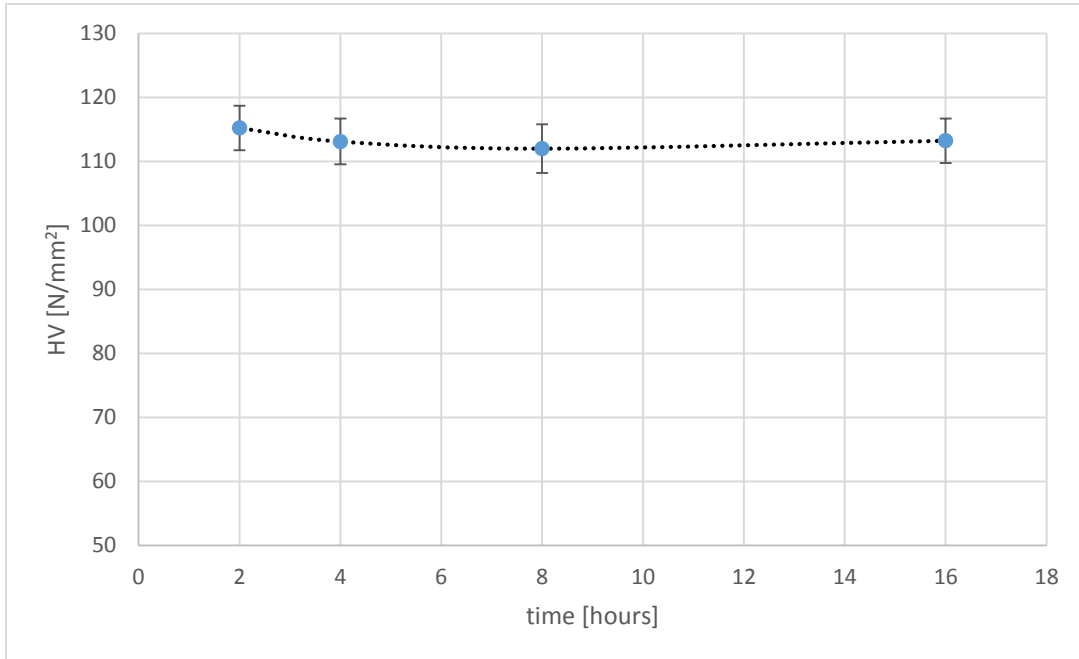


Fig. 3.15: Hardness of WE43 8P annealed at 250 °C

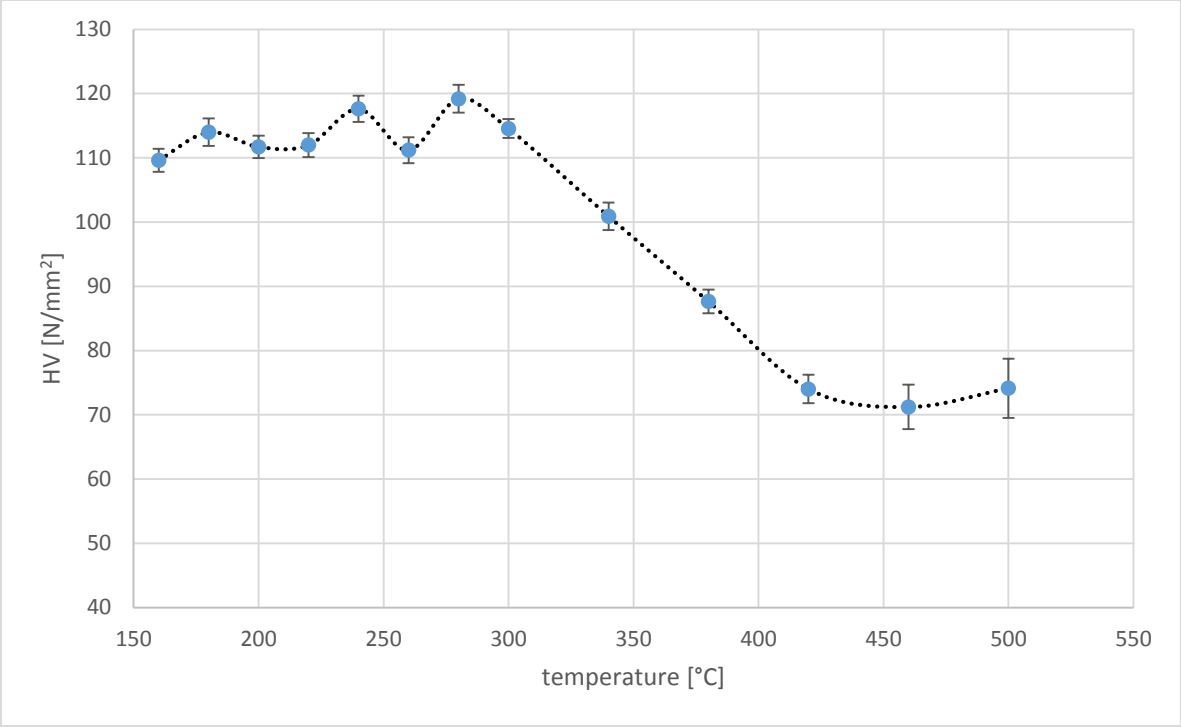


Fig. 3.16: Hardness of WE43 8P annealed for 1 hour.

4. Discussion

The effect of ultrafine-grained structure on the mechanical properties of WE43 was investigated, with the grain size dropping down to approximately 340 nm in case of 8 ECAP passes [24]. Our measurement of the grain size of WE43 AC resulted in 115 μm , thus constituting a difference of 3 orders of magnitude.

The main sources of the material strengthening are grain boundary strengthening and precipitation hardening. The grain boundary's strengthening effect is calculated by Hall-Petch equation (Eq. 1.1), where yield stress is dependent on $d^{-1/2}$ down to a cap of 10 nm, at which point the grain boundary begins to slide [26]. Until that point, the grain boundary proves to be an effective barrier against dislocation movement, successfully impeding it and causing dislocations to pile up. The precipitation hardening mechanism depends on the coherency and size of the precipitate. If a precipitate is coherent the dislocation can cut through it, continuing on the same slip plane. In case of an incoherent precipitate, the dislocation bows out around the precipitate until it bows sufficiently so that the two bowed out parts of the dislocation meet and annihilate, leaving a dislocation loop around the precipitate and continuing its movement further. The dislocation loops left behind create a stress field, further impeding the movement of dislocations.

We would thus expect the value of yield strength to increase with a decrease in grain size due to grain boundary strengthening. The results were in accordance with this expectation (Table 1). The increase in yield strength was accompanied by a significant increase in Young's modulus (uniaxial stress divided by strain), resulting in increased strength and reduced ductility (Fig. 3.10), however the WE43 8P still reached an impressive value of 13% ϵ in both tension and compression, considering that its yield strength surpassed 400 MPa. We would also expect the yield strength to increase after annealing, due to the formation of precipitates (Fig. 3.8j) and subsequent precipitation hardening, with the results being in accordance with our prediction.

The evolution of hardness of the WE43 annealed at 210 °C and 250 °C shows noticeable differences. The reasoning behind this is the difference in formation of precipitates in the material under different temperatures. While at 210 °C the formation of lamellas is very slow (Fig. 3.6) with the hardness of the material peaking at 3 days, at 250 °C substantial amount of lamellas is present in the sample after just 4 hours of annealing (Fig. 3.8c), with highest hardness achieved after just 8 hours. One can actually observe 3 main types of phases that appear in the material in (Fig. 3.8c). The first one being β' in the shape of tiny discs/globulars, the second one being β_1 with a plate-like shape, appearing on the right side of the grain boundary as medium sized lamellas, and finally β with a rod-like shape appearing at the left side of the grain boundary as long lamellas. The β' are very small and they fill the remainder of the figure. Since β' phase significantly increases hardness of a material while β , being an incoherent phase, does not. Since WE43 annealed at 250 °C has a considerable amount of β phase from early stages, it is not surprising that its hardness is lower than that of the one annealed at 210 °C.

Of particular interest is the thermal stability of the ultrafine-grained structure present in WE43 8P, which shows good thermal stability when annealed at 250 °C (temperature of T5 temper) from 2 to 8 hours (Fig 3.15). When annealed isochronally for 1 hour, the structure remains fairly stable up to temperature of around 300 °C, with hardness falling sharply after that point. Because the precipitates are already present after ECAP, elevating the temperature above certain point (in our case 300 °C) causes dissolution of the precipitates, and the subsequent loss of precipitation hardening. The precipitates found in the material are Mg_5RE particles with FCC structure (Fig. 3.6) [24]. Recent study also showed an increase in average grain size past the temperatures of 300 °C, which further reduces the hardness of the material [24]. The reduction in grain boundary strengthening as well as precipitation hardening leads to the profound reduction in hardness of the material, as seen in Fig. 3.16, with the hardness dropping almost to half of its maximum value.

5. Conclusion

The effect of substantial grain refinement of WE43 magnesium alloy, along with the thermal stability of formed microstructure.

- Processing by ECAP caused a significant grain refinement and precipitation. Grain size decreased from $\sim 115 \mu\text{m}$ to $\sim 340 \text{ nm}$, a three orders of magnitudes reduction.
- Yield strength of the material in compression increased based on the number of ECAP passes with 8 passes reaching the value of $\sim 412 \text{ MPa}$ – a more than 3 times the value of the AC state. WE43 8P was also tested in tension with the result of $\sim 364 \text{ MPa}$. Along with this high yield strength, WE43 8P also displayed the ability to stretch more than 13% in both tension and compression, making surprisingly ductile considering its high yield strength.
- Investigation of thermal stability of AC state at $210 \text{ }^\circ\text{C}$ and $250 \text{ }^\circ\text{C}$ showed the effect of second phase particles on the hardness of the material, with $210 \text{ }^\circ\text{C}$ showing superior results with the maximum hardness being $\sim 101 \text{ HV}$.
- Ultrafine-grained structure of WE43 8P showed good thermal stability while being annealed at $250 \text{ }^\circ\text{C}$ from 2-8 hours. During isochronal annealing for 1 hour, the structure maintained its stability up to $300 \text{ }^\circ\text{C}$. Further temperature increase led to a sharp fall of microhardness from a maximum of $\sim 120 \text{ HV}$ to a minimum of $\sim 71 \text{ HV}$ which was caused by dissolution of precipitates and increase of grain size.

Bibliography

- [1] M.M. Avedesian, H. Baker *Magnesium and Magnesium Alloys*. ASM international (1999)
- [2] B.L. Mordike, T. Ebert. *Magnesium: properties — applications — potential*. Mater. Sci. Eng.A, 302 (2001), pp. 37-45, 10.1016/S0921-5093(00)01351-4
- [3] N.S. Martynenko, E.A. Lukyanova, V.N. Serebryany, M.V. Gorshenkov, I.V. Shchetinin, G.I. Raab, S.V. Dobatkin, Y. Estrin, *Increasing strength and ductility of magnesium alloy WE43 by equal-channel angular pressing*, *Materials Science and Engineering: A*, Volume 712, 2018, Pages 625-629, ISSN 0921-5093
- [4] Elena Lukyanova, Natalia Anisimova, Natalia Martynenko, Mikhail Kiselevsky, Sergey Dobatkin, Yuri Estrin, *Features of in vitro and in vivo behaviour of magnesium alloy WE43*, *Materials Letters*, Volume 215, 2018, Pages 308-311, ISSN 0167-577X,
- [5] Y.F. Zheng, X.N. Gu, F. Witte. *Biodegradable metals* Mater. Sci. Eng. R., 77 (2014), pp. 1-34
- [6] Katarzyna Świrk, Maria Elena Gálvez, Monika Motak, Teresa Grzybek, Magnus Rønning, Patrick Da Costa, *Yttrium promoted Ni-based double-layered hydroxides for dry methane reforming*, *Journal of CO2 Utilization*, Volume 27, 2018, Pages 247-258, ISSN 2212-9820,
- [7] Naemi A. Zumdick, Lucas Jauer, Lisa C. Kersting, Tatiana N. Kutz, Johannes H. Schleifenbaum, Daniela Zander, *Additive manufactured WE43 magnesium: A comparative study of the microstructure and mechanical properties with those of powder extruded and as-cast WE43*, *Materials Characterization*, Volume 147, 2019, Pages 384-397, ISSN 1044-5803,
- [8] Sahithya Kandalam, Priyanka Agrawal, G.S. Avadhani, S. Kumar, Satyam Suwas, *Precipitation response of the magnesium alloy WE43 in strained and unstrained conditions*, *Journal of Alloys and Compounds*, Volume 623, 2015, Pages 317-323, ISSN 0925-8388,
- [9] J. Orlikowski, K. Darowicki, *Investigations of pitting corrosion of magnesium by means of DEIS and acoustic emission* *Electrochim. Acta*, 56 (2011), pp. 7880-7884
- [10] G.T. Burstein, C. Liu, *Nucleation of corrosion pits in Ringer's solution containing bovine serum* *Corros. Sci.*, 49 (2007), pp. 4296-4306
- [11] Michal Knapek, Peter Minárik, Jan Čapek, Robert Král, Jiří Kubásek, František Chmelík, *Corrosion of pure magnesium and a WE43 magnesium alloy studied by advanced acoustic emission analysis*, *Corrosion Science*, Volume 145, 2018, Pages 10-15, ISSN 0010-938X
- [12] L. Tang, Y. Zhao, R.K. Islamgaliev, R.Z. Valiev, Y.T. Zhu *Microstructure and thermal stability of nanocrystalline Mg-Gd-Y-Zr alloy processed by high pressure torsion* *J. Alloys Compd.*, 721 (2017), pp. 577-585

- [13] F. Dalla Torre, R. Lapovok, J. Sandlin, P.F. Thomson, C.H.J. Davies, E.V. Pereloma *Microstructures and properties of copper processed by equal channel angular extrusion for 1–16 passes* Acta Mater, 52 (2004), p. 4819
- [14] Peter Minárik, Robert Král, Jakub Čížek, František Chmelík, *Effect of different c/a ratio on the microstructure and mechanical properties in magnesium alloys processed by ECAP*, Acta Materialia, Volume 107, 2016, Pages 83-95, ISSN 1359-6454,
- [15] Terence G. Langdon, *Twenty-five years of ultrafine-grained materials: Achieving exceptional properties through grain refinement*, Acta Materialia, Volume 61, Issue 19, 2013, Pages 7035-7059, ISSN 1359-6454
- [16] Lingling Tang, Yonghao Zhao, R.K. Islamgaliev, R.Z. Valiev, Y.T. Zhu, *Microstructure and thermal stability of nanocrystalline Mg-Gd-Y-Zr alloy processed by high pressure torsion*, Journal of Alloys and Compounds, Volume 721, 2017, Pages 577-585, ISSN 0925-8388
- [17] Základní fyzikální praktikum MFF UK, *Určení strukturálních parametrů krystalických látek metodami skenovací elektronové mikroskopie (SEM)*, [reference 12/14/2018], available from: <https://physics.mff.cuni.cz/vyuka/zfp/zadani/418>
- [18] Ray F. Egerton, *Physical Principle of Electron Microscopy*, New York, Springer Science+Business Media, 2005
- [19] Official Instron website *Vickers test* [reference 12/21/2018] available from: <http://www.instron.us/en-us/our-company/library/test-types/hardness-test/vickers-test>
- [20] A. Tricoteaux, E. Rguiti, D. Chicot, L. Boilet, M. Descamps, A. Leriche, J. Lesage, *Influence of porosity on the mechanical properties of microporous β -TCP bioceramics by usual and instrumented Vickers microindentation*, Journal of the European Ceramic Society, Volume 31, Issue 8, 2011, Pages 1361-1369, ISSN 0955-2219
- [21] Základní fyzikální praktikum MFF UK, *Dynamická zkouška deformace látek v tlaku*, [reference 11/19/2018], available from: https://physics.mff.cuni.cz/vyuka/zfp/_media/zadani/texty/txt_111.pdf
- [22] A. Alavudeen, N. Venkateshwaran, J. T. Winowlin Jappes. *A Textbook of Engineering Materials and Metallurgy*. New Delhi: LAXMI PUBLICATIONS (P) LTD, 2006
- [23] Peter Minárik, Jozef Veselý, Robert Král, Jan Bohlen, Jiří Kubásek, Miloš Janeček, Jitka Stráská, *Exceptional mechanical properties of ultra-fine grain Mg-4Y-3RE alloy processed by ECAP*, Materials Science and Engineering: A, Volume 708, 2017, Pages 193-198, ISSN 0921-5093
- [24] Peter Minárik, Jozef Veselý, Jakub Čížek, Mária Zemková, Tomáš Vlasák, Tomáš Krajňák, Jiří Kubásek, Robert Král, Daniel Hofman, Jitka Stráská, *Effect of secondary phase particles on thermal stability of ultra-fine grained Mg-4Y-3RE alloy prepared by equal channel angular pressing*, Materials Characterization, Volume 140, 2018, Pages 207-216, ISSN 1044-5803
- [25] E. Bertrand, P. Castany, I. Péron, T. Gloriant, *Twinning system selection in a metastable β -titanium alloy by Schmid factor analysis*, Scripta Materialia, Volume 64, Issue 12, 2011, Pages 1110-1113, ISSN 1359-6462

[26] Chun Yee Aaron Ong, Daniel John Blackwood, Yi Li, *The effects of W content on solid-solution strengthening and the critical Hall-Petch grain size in Ni-W alloy*, *Surface and Coatings Technology*, Volume 357, 2019, Pages 23-27, ISSN 0257-8972

List of Tables

Table 1 Yield stress of tested materials in compression.....	30
--	----

List of Figures

Fig. 1.1 Principle of ECAP.	10
Fig. 2.1 Principle of channeling contrast.	14
Fig. 2.2 Tensile strength test specimen.	19
Fig. 3.1 WE43 AC photographed using optical microscopy.....	21
Fig. 3.2 SEM images of WE43.	22
Fig. 3.3 SEM images of WE43 4P.	23
Fig. 3.4 SEM images of WE43 8P.	23
Fig. 3.5 Detail of Zr particles in WE43 8P.	24
Fig. 3.6 TEM image of WE43 8P sample (bright field) with SAED pattern of Mg ₃ RE.....	25
Fig. 3.7 WE43 isothermally annealed at 210 °C.....	27
Fig. 3.8 WE43 AC annealed at 250 °C	28
Fig. 3.9 WE43 AC annealed for 1 hour.....	29
Fig. 3.10 Stress-strain diagram (compression) for WE43 AC, 4P, 8P and WE43 AC T5.....	30
Fig. 3.11 Stress-strain diagram (tension) for WE43 8P.	31
Fig. 3.12 SEM photo of a plastically deformed WE43 8P.	32
Fig. 3.13 Hardness of WE43 AC annealed at 210 °C.....	33
Fig. 3.14 Hardness of WE43 AC annealed at 250 °C.	33
Fig. 3.15 Hardness of WE43 8P annealed at 250 °C.....	34
Fig. 3.16 Hardness of WE43 8P annealed for 1 hour.	35

List of Abbreviations

WE43	magnesium alloy with composition {Mg, Y (3.56%), Nd (2.20%), Zr (0.47%)}
SEM	scanning electron microscopy
TEM	transmission electron microscopy
RE	rare earths
SPD	severe plastic deformation
ECAP	equal channel angular press
UFG	ultrafine-grained
BSE	backscattered electrons
SE	secondary electrons
HV	Vickers Pyramid Number
AC	as-cast
4P, 8P	4, 8 ECAP passes
HCP	hexagonal close-packed